THE ASTROPHYSICAL JOURNAL, 474:329–345, 1997 January 1
© 1997. The American Astronomical Society. All rights reserved. Printed in U.S.A.

A STUDY OF THE MUTUAL INTERACTION BETWEEN THE MONOCEROS R2 OUTFLOW AND ITS SURROUNDING CORE

M. TAFALLA
Radio Astronomy Laboratory, University of California at Berkeley, 901 Campbell Hall, Berkeley, CA 94720 and
Harvard-Smithsonian Center for Astrophysics, MS 42, 60 Garden Street, Cambridge, MA 02138[1];
tafalla@cfa.harvard.edu

R. BACHILLER
Observatorio Astronómico Nacional, Campus Universitario, Apartado 1143, E-28800,
Alcalá de Henares (Madrid), Spain; bachiller@cay.es

AND

M. C. H. WRIGHT AND W. J. WELCH
Radio Astronomy Laboratory, University of California at Berkeley, 601 Campbell Hall, Berkeley, CA 94720
Received 1996 March 14; accepted 1996 July 18

ABSTRACT

We present high-resolution (12″–24″) ^{12}CO(J = 2–1), ^{13}CO(2–1), CS(2–1), CS(3–2), and CS(5–4) maps of the central 4′ × 4′ of Mon R2 and study the bipolar outflow, the dense core, and their mutual interaction. The high-velocity ^{12}CO and ^{13}CO emissions that trace the bipolar outflow show that the outflow lobes are limb-brightened shells of accelerated gas that have the Mon R2 IR cluster near their apex and extend approximately toward the north and south. These shells of gas are clumpy, and their emission at the highest velocities arises from discrete condensations that move with the flow but each has a slightly different speed. The CS data, on the other hand, trace the ambient core at low velocities, but also trace the accelerated gas of the outflow at higher speeds. The ambient CS emission shows that the core has a cavity along the path of the outflow, and that the walls of this cavity coincide in position and orientation with the shells of the bipolar flow. The accelerated CS emission concentrates along the cavity walls and arises from the same clumpy shells of gas that form the outflow lobes in ^{12}CO and ^{13}CO. This outflow material, therefore, is rather dense, and a solution of the CS radiative transfer shows that it is as dense as the gas in the core ($\approx 4 \times 10^5$ cm^{-3}), suggesting that what we see as outflow is in fact gas from the dense core that has been set into motion.

With the same radiative transfer analysis of the CS lines, we estimate that from a total of 1000 $M_\odot$ of dense gas in the core, more than 170 $M_\odot$ have been accelerated and incorporated into the bipolar flow. In addition, the CS spectra show a systematic enhancement of the line width toward the IR cluster that suggests the outflow has increased the gas turbulence in its vicinity. The amount of kinetic energy contained in both the bipolar and turbulent motions is comparable to the total binding energy of the dense gas, and this shows that the action of the outflow on the core can be strong enough to affect the distribution of dense gas in the core. We therefore propose that the cavity in the dense gas is the result of the evacuation of a channel by the outflow, and that the material initially filling its volume has been accelerated and incorporated into the flow. The Mon R2 system, therefore, illustrates how bipolar molecular outflows form through the acceleration of ambient molecular gas and that the process of molecular outflow formation is accompanied by a partial destruction of the dense gas environment of the newly formed star.

Subject headings: ISM: individual (Monoceros R2) — ISM: jets and outflows — ISM: kinematics and dynamics — stars: formation

1. INTRODUCTION

Bipolar molecular outflows were first identified more than a decade and a half ago (Snell, Loren, & Plambeck 1980) and by now they have been found around almost any nearby young stellar object (see Bachiller 1996 for a recent review and Fukui et al. 1993 for a catalog of outflows). This ubiquity suggests that the outflow phase is an essential part of the star formation process, and that stars of all masses go through this phase at an early stage in their lives (see, e.g., Lada 1985). Bipolar outflows, in addition, are very energetic phenomena. The high-velocity molecular gas observed in outflows (mostly through its CO emission) represents an appreciable fraction of the ambient material from the stellar vicinity that has been swept up by a strong stellar wind (Snell 1987). Outflows therefore represent strong perturbations of the environment around newly born stars, and this together with their ubiquity implies that the outflow phenomenon can affect the evolution of star-forming material near newly born stars. How outflows perturb the environment, however, is not yet well understood. This is unfortunate because understanding how outflows interact with their surroundings is a necessary step in understanding both the evolution of gas around young stars as well as the acceleration of the molecular component of the outflow which is finally observed in CO (the underlying driving wind may have been observed in some special cases, but in atomic form, see Lizano et al. 1988). It seems therefore important to investigate the interaction of bipolar outflows and their environment, both from the observational as well

[1] Present address.

as from the theoretical point of view. In this paper we present an observational study of the Mon R2 molecular outflow and its interaction with the surrounding core. Because of the extreme parameters of the Mon R2 outflow (one of the oldest and most massive outflows known, see below), this system represents an ideal case to study the long-term effect of an outflow on the surrounding ambient material and, at the same time, to explore the mechanism of acceleration of molecular gas that forms a typical CO outflow.

The Mon R2 star-forming core, at a distance of 950 pc (Racine & van den Bergh 1970), was first identified by Kutner & Tucker (1974) because of its strong molecular emission (see also Loren, Peters, & Vanden Bout 1974 and Kutner & Tucker 1975). It contains an embedded IR cluster (Beckwith et al. 1976) of total luminosity around 5×10^4 $L_\odot$ (Thronson et al. 1980) and an optically invisible H II region (Downes et al. 1975). The main sources of the cluster, IRS 1, 2, and 3 (notation of Beckwith et al. 1976), lie within the central 30″ of the dense core, and while IRS 1 is considered the exciting source of the H II region (Gilmore 1980; Massi, Felli, & Simon 1985), IRS 2 seems to excite a spherical reflection nebula (Hodapp 1987; Aspin & Walther 1990a). Recent large-scale K-band images by Aspin & Walther (1990b) have revealed many more sources embedded in the core, showing that the total population of the cluster is of the order of several hundred and that its extension encompasses several arcminutes in diameter.

Mapping the CO emission from Mon R2, Loren (1977) found high-velocity gas distributed bipolarly with respect to the IR cluster. This gas was later identified as resulting from a molecular outflow (Loren 1981), which has been characterized in detail by the large-scale observations of Wolf, Lada, & Bally (1990) and Meyers-Rice & Lada (1991). Wolf et al. (1990) estimate that the molecular outflow extends over 25′ (7 pc) and contains more than 200 $M_\odot$ of accelerated gas. These parameters indicate that Mon R2 is one of the most extreme outflows known, probably the result from a combination of the high luminosity of its exciting source and the large kinematical (and probably physical) age of the flow (1.5×10^5 yr; Wolf et al. 1990) that has given the outflow enough time to sweep up a large amount of ambient gas.

The dense gas in the Mon R2 core has been mapped with high-dipole molecules like CS (Kutner & Tucker 1975; Heyer et al. 1986; Wolf et al. 1990; Montalbán et al. 1990; Xie 1992), NH_3 (Willson & Folch-Pi 1981; Torrelles et al. 1983; Torrelles et al. 1990; Montalbán et al. 1990), and HCO^+ (Richardson et al. 1988; Gonatas, Palmer, & Novak 1992). Those observations with high enough angular resolution (less than 60″) find that the emission does not peak exactly at the position of the brightest IR sources but presents two separate peaks east and west of the stars. The observations, in addition, show that there is a slight change in velocity across the dense core (≈ 1 km s^{-1}), which has been commonly interpreted as evidence for rotation (Torrelles et al. 1983; Richardson et al. 1988; Wolf et al. 1990). Despite all these existing observations, however, no simultaneous study of the Mon R2 outflow and dense core has been carried out so far, and no attempt to relate the dense gas velocity field with the bipolar outflow pattern has been done. This is unfortunate because the Mon R2 outflow, with its enormous size and mass, is expected to have perturbed a large fraction of its immediate surroundings, and for this reason in this paper we explore this possibility, presenting new high-resolution observations of both outflow and dense gas tracers.

2. OBSERVATIONS

We observed the CS($J = 2$–1), CS(3–2), CS(5–4), and ^{12}CO(2–1) transitions toward the Mon R2 core with the IRAM 30 m telescope in 1990 June 16–18, simultaneously using receivers at 1, 2, and 3 mm. During the first part of the observation, the three receivers were tuned to the three CS lines, and every other point on a 20″ grid was observed. Afterward, the 1 mm receiver was retuned to ^{12}CO(2–1), and the remaining points of the grid were observed with the new receiver configuration. As a result of this change, we obtained two maps with 20″ sampling in CS(2–1) and CS(3–2), and two maps with $20(2)^{1/2}$″ sampling in CS(5–4) and ^{12}CO(2–1). All the observations were done in position switching mode with the reference position about 10′ away from the Mon R2 center. This position was free from CS emission but not from ^{12}CO(2–1) because of the large extension of the cloud. The ^{12}CO(2–1) lines are therefore contaminated at low velocities, and the ambient ^{12}CO will not be discussed here.

For the two lowest CS transitions, the telescope beam size was 24″ and 16″, and for both CS(5–4) and ^{12}CO(2–1), the beam size was ≈ 11″. The spectrometers were an autocorrelator with 1024 channels covering a total band width of 40 MHz for CS(2–1), a filter bank of 512×100 kHz channels for CS(3–2), and a 256×1 MHz filter bank for both CS(5–4) and CO(2–1). They provided velocity resolutions of 0.12, 0.20, 1.2, and 1.3 km s^{-1} for CS(2–1), CS(3–2), CS(5–4), and ^{12}CO(2–1), respectively.

We checked the antenna pointing frequently by making cross scans on Jupiter and Mercury, and we found it accurate within 3″ (rms). We also checked the relative calibration by repeated observations of selected Mon R2 positions, finding no changes throughout the observations. To check the absolute calibration, we observed several standards from the catalog of Mauersberger et al. (1989). Our CS(3–2) and ^{12}CO(2–1) spectra were in good agreement with those in the catalog, and no further correction was applied. Our CS(2–1) spectra from TMC1(HC5N) and IRC +10216, however, were consistently brighter than those in the catalog, so we divided our CS(2–1) intensities by 1.65. No calibrated CS(5–4) spectra are available in the Mauersberger et al. catalog, so no correction was applied to the CS(5–4) data. The results in this paper are expressed in units of $T_{\rm mb}$, where the main beam efficiencies were assumed to be 0.6, 0.6, and 0.45 for 3, 2, and 1 mm, respectively (Mauersberger et al. 1989).

Our ^{13}CO (2–1) observations were carried out with the JCMT[2] during the nights of 1993 January 28–31. We mapped the central 4′ × 4′ with 20″ sampling and covered a surrounding region with $20(2)^{1/2}$″ sampling. The observations were done in position switching mode with the reference position 20′ east of the map center. This position emits a narrow ($\Delta V = 0.9$ km s^{-1}), weak ($T_{\rm mb} = 2.3$ K) ^{13}CO(2–1) line, so the observed spectra were contaminated by this emission. To correct for this contamination, a high signal-to-noise spectrum of (20′, 0) was obtained (in posi-

[2] The James Clerk Maxwell Telescope (JCMT) is operated by The Observatories on behalf of the Particle Physics and Astronomy Research Council of the United Kingdom, the Netherlands Organisation for Scientific Research, and the National Research Council of Canada

tion switching mode with respect to a further, clean position) and the result added to the data.

The backend was an acousto-optical spectrometer with 500 MHz of total bandwidth and a velocity resolution of about 0.34 km s^{-1}. The telescope beam size was $\sim 21''$. The pointing was checked frequently by continuum cross scans of the central position of Orion (IRC2) and was better than $1''.5$ (rms). Calibration was checked by taking ^{13}CO (2–1) spectra of Orion (IRC2) and the center of Mon R2. It was found to be consistent during each day within 5% (rms), but some systematic day-to-day variations ($\sim 10\%$) were observed. The day-to-day variations were later corrected by scaling the spectra of different days by the appropriate factors, and the absolute scale was set assuming the ^{13}CO (2-1) peak antenna temperature of Orion (IRC2) is 34.6 K (the average of all our spectra). The T_A^* scale from the telescope was converted into T_{mb} scale using a beam efficiency of 0.71 (Davies 1992).

3. RESULTS

3.1. *Results from* ^{13}CO *Observations*

In order to better understand the kinematics of ^{13}CO, we will study the emission in three stages, gradually increasing the velocity resolution. First, we present the integrated map and discuss the overall gas distribution. Next, we study "broadband" maps and separate the outflow emission from the ambient component, and, finally, we present detailed velocity maps and discuss the clumpy nature of the emitting gas.

3.1.1. *Integrated Emission: The Mon R2 Core*

Figure 1 shows the map of ^{13}CO (2–1) emission integrated from 0 to 21 km s^{-1}, where most of the signal is detected. The distribution of ^{13}CO presents two bright condensations separated by a relative minimum toward the position of IRS 1 and 2 (indicated by two stars near the map center). Each of these condensations east and west of IRS 1-2 contains several maxima, and one of them coincides with the embedded object IRS 3 ($\approx 30''$ east of IRS 1-2). A region of relatively low ^{13}CO (2–1) emission around IRS 1-2 extends toward the northwest and runs between the two condensations. This elongated region will be referred hereafter as the "emission valley," and, as we will see in further sections, it coincides with the path of the bipolar outflow.

The distribution of the Mon R2 emission in two condensations separated by a valley is not peculiar to ^{13}CO (2–1). The ^{12}CO(1–0), HCN(1–0), and HCO^+(1–0) maps of

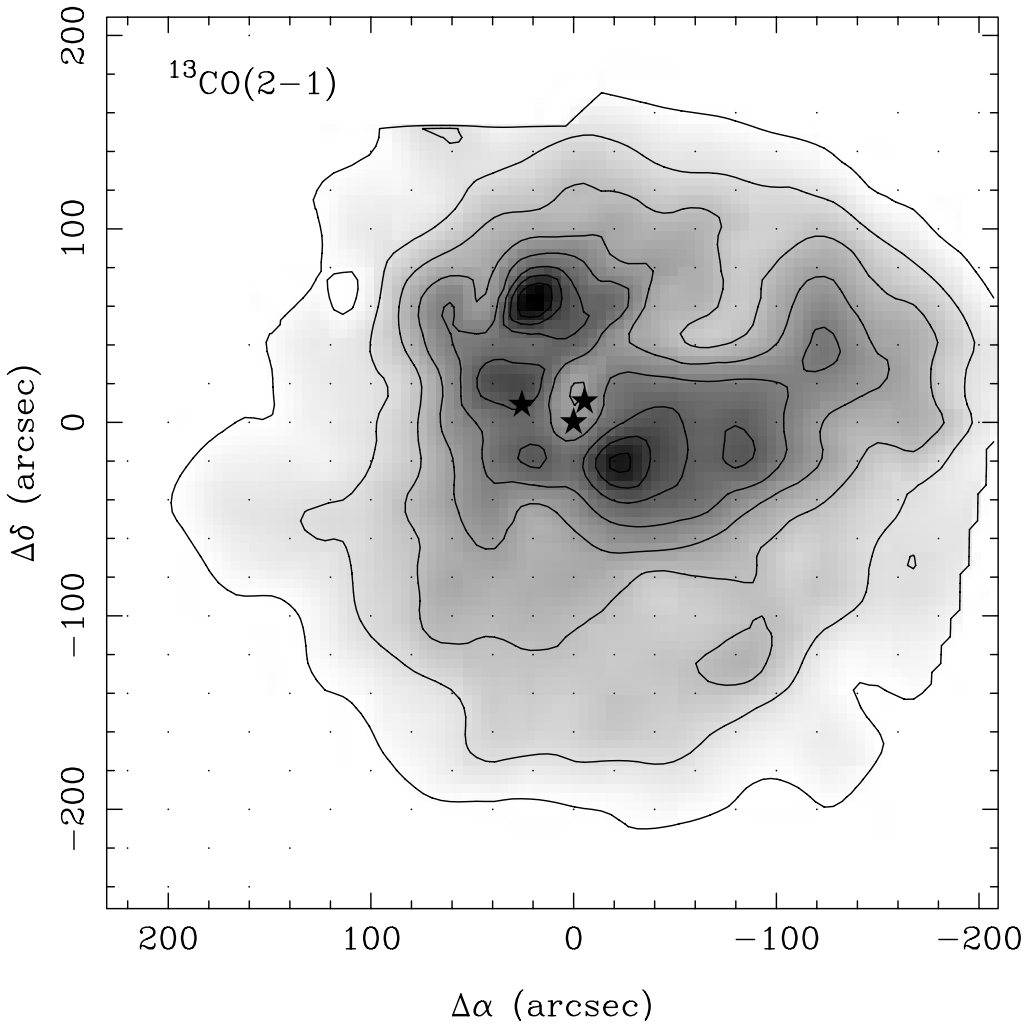


FIG. 1.—Map of ^{13}CO(2–1) mean beam brightness temperature integrated from 0 to 21 km s^{-1}. The offsets are referred to the position of the VLA 6 cm peak of Massi et al. (1985) ($\alpha_{1950} = 06^h05^m20^s$, $\delta_{1950} = -06°22'39''.4$) The stars indicate the location of IRS1, IRS2, and IRS3, that lie at ($-3''$, $1''.4$), ($-8''.9$, $15''.4$), and ($22''.4$, $13''.4$), respectively (Hackwell, Grasdalen, & Gehrz 1982). The contours are at 20%, 30%, ..., 90% of the peak integrated intensity (= 140 K km s^{-1}).

Richardson et al. (1988), the NH_3 maps of Montalbán et al. (1990), and the CS maps of § 3.3.1 (see also Heyer et al. 1986 and Xie 1992) all show the emission from the Mon R2 core consists of two condensations at each side of IRS 1-2. This agreement between different molecular tracers rules out the possibility that the ^{13}CO(2–1) brightness distribution results from an anomalous excitation at the center of the core (no evidence for self-absorption is found in the ^{13}CO spectra, for example) and suggests there is a real decrease in molecular gas along the emission valley.

3.1.2. *Broadband Kinematics: the Outflow Shells*

As a second step in our study, we divide the same velocity range of Figure 1 into three broad components (ambient cloud, red regime, and blue regime) and present their maps in Figure 2. The ambient cloud is centered at $V_{LSR} = 10.5$ km s^{-1}, the velocity of the average ^{13}CO (2–1) spectrum, and covers the central 4 km s^{-1}. The blue regime consists of velocities lower than 8.5 km s^{-1}, and the red regime contains velocities larger than 12.5 km s^{-1}. As the maps show, the blue gas extends northwest of the IR cluster and the red gas lies mostly to the south, forming a bipolar distribution that agrees well with the large-scale distribution of the ^{12}CO outflow studied by Loren (1977), Wolf et al. (1990), and Meyers-Rice & Lada (1991). The blue and red broad regimes of ^{13}CO (2–1), therefore, correspond to the blue and red lobes of the Mon R2 bipolar outflow.

The blueshifted gas (*left panel*) forms an arc toward the northwest that resembles the gas distribution found in other outflows like L1551 (see, e.g., Moriarty-Schieven et al. 1987; Uchida et al. 1987) and NGC 2071 (see, e.g., Moriarty-Schieven, Snell, & Hughes 1989). Such distributions are usually interpreted as limb-brightened shells of accelerated material, and this interpretation also seems valid for Mon R2. In fact, although no previous observations have spatially resolved the Mon R2 outflow into shells, the study of position-velocity diagrams by Meyers-Rice & Lada (1991) had already suggested the Mon R2 outflow consists of accelerated shells, like L1551 and NGC 2071. Our observations show these shells are very clumpy (see below).

The ambient map (*middle panel*) resembles the integrated map of Figure 1 and shows the two condensations surrounding the IR cluster with the emission valley in between. The map, however, does not present as much contrast as the maps of accelerated gas, suggesting the ambient emission suffers from moderate saturation.

Finally, the redshifted ^{13}CO (*right panel*) has a triangular distribution with the top vertex near IRS 1-2 and the base toward the south. This red emission arises from outflow gas, and the triangular distribution suggests the flow originates near the IR cluster and diverges as it moves south. Our latter study of the narrow velocity maps and the modeling of their emission will show that the redshifted gas also forms a well defined shell; it is the larger mass of the red outflow and its larger optical depth that makes the red shell less obvious in the broadband maps.

3.1.3. *Detailed Kinematics: Clumps and Third Dimension of the Southern Shell*

As a final step in our study of the ^{13}CO (2–1) kinematics, we present in Figure 3 a series of maps integrated every 2 km s^{-1}. These maps illustrate the clumpy nature of the outflow and give clues to the three-dimensional geometry of the southern shell.

The bluest maps of Figure 3 (first three panels with $V < 8$ km s^{-1}) show that the different maxima in the blue broadband shell arise from different clumps that move at slightly different velocities. The first two maps, in particular, show that the bluest emission concentrates in two distinct clumps located at about (−140″, 40″) and (0, 0). These clumps represent the most prominent members of a whole clump family that, as we will see in § 3.3.3, comprise most of the outflow material. The properties of these clumps have been discussed in Tafalla, Bachiller, & Wright (1994) using a CS multitransitional analysis, and the clumps in the first two ^{13}CO maps correspond to clumps B and C in the notation of that paper.

The two ambient maps ($8 < V < 10$ and $10 < V < 12$) suffer from moderate optical depth and present less contrast than the others. Still, they show that the emission shifts from north to south with increasing velocity, following the bipolarity of the outflow.

The red maps, especially those with $V > 14$ km s^{-1}, show a systematic velocity pattern in the outflow emission: the red gas starts as a limb-brightened shell south of the IR cluster ($14 < V < 16$ panel), and as the velocity increases, the shell walls approach each other ($16 < V < 18$) and finally merge forming an elongated feature that seems to

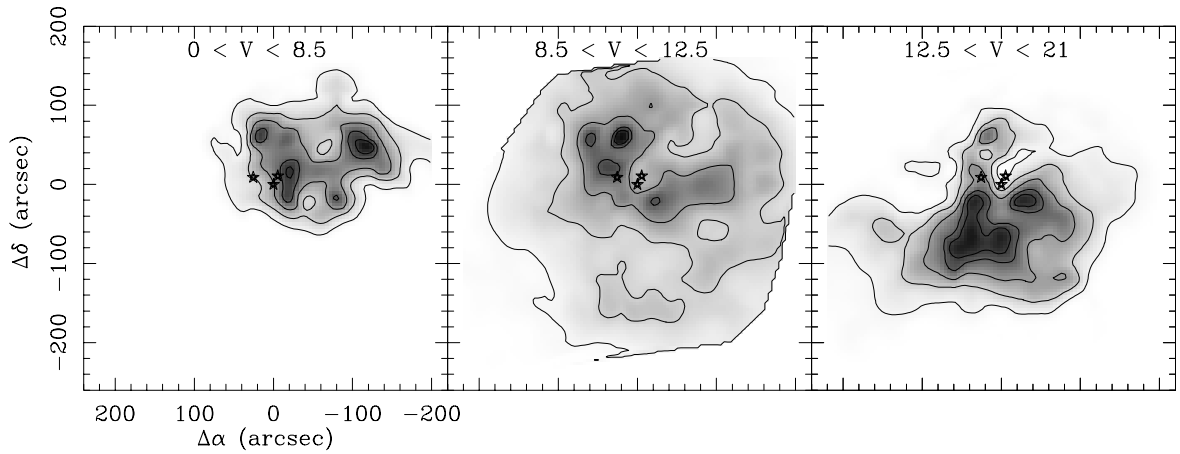


FIG. 2.—Broadband ^{13}CO(2–1) velocity maps of Mon R2. The velocity range of each map is indicated in the top of the panel. Contours are at 20%, 40%, …, 80%, and 90% of the map maximum, and the maxima are 33.5, 87.8, and 33.0 K km s^{-1} for the blue, ambient, and red regimes, respectively. Map centers and stars as in Fig. 1.

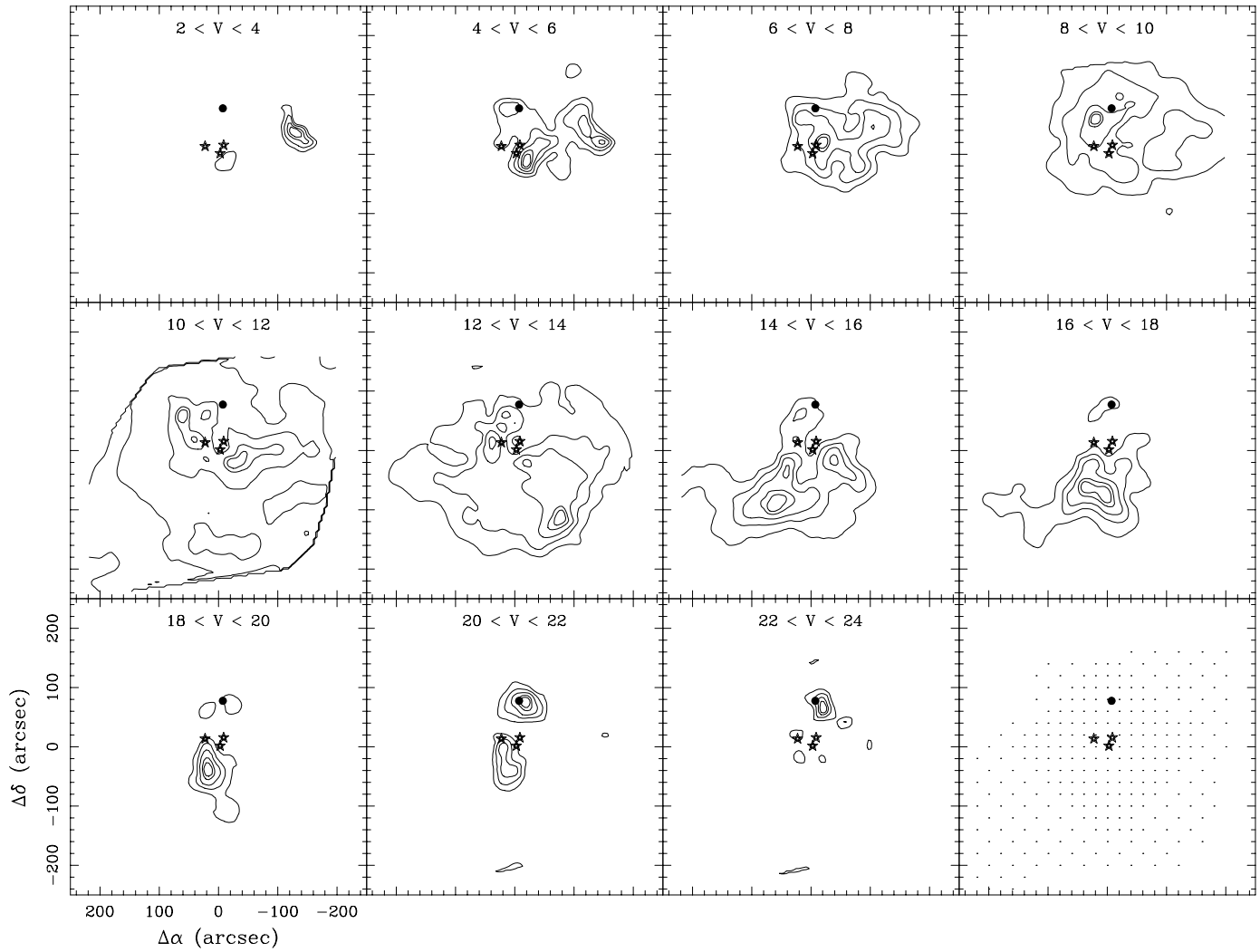


FIG. 3.—Maps of ^{13}CO(2–1) intensity integrated every 2 km s^{-1}. The contours of each panel are at 20%, 40%, 60%, 80%, and 90% of the map maximum, except for the two most extreme velocity panels, where the 20% contour was excluded because of low signal to noise. (Map maxima, for increasing velocity intervals, are: 1.5, 8.4, 23.0, 55.1, 42.2, 25.9, 15.4, 10.1, 7.1, 2.3, and 1.2 K km s^{-1}.) Map centers and stars as in Fig. 1. The filled circle at (−7″.5, 77″.5) indicates the position of Cohen & Frogel's (1977) Object 1.

emanate from the IR cluster and runs south along the shell axis ($18 < V < 20$). At these highest velocities, a separate condensation appears to the north of the cluster, at about (20″, 80″) and becomes the brightest feature in the last two maps. This northern condensation violates the bipolar distribution of the accelerated gas and coincides in position with a very red star referred by Cohen & Frogel (1977) as Object 1 (their brightest) in a 9400 Å photograph of the Mon R2 region. More recent *K*-band images by Aspin & Walther (1990b) and Hodapp (1994) show diffuse nebulosity surrounding this source, confirming its association with the molecular cloud. We interpret the anomalous red gas to the north of the cluster as arising from a second molecular outflow, probably excited by Cohen & Frogel's Object 1, and we will refer to it as Mon R2-N. Because of the extremely bright emission of the more massive main Mon R2 outflow, Mon R2-N is only visible at the most extreme red velocities, when the contribution of the main outflow disappears.

The transition from shell to centrally concentrated geometry at low-red velocities occurs so gradually that it very likely arises from a systematic pattern in the outflow velocity field. One possibility is that the gas along the outflow axis moves faster than the gas near the walls, as it occurs in a shear flow. Another possibility, that we favor because it keeps the symmetry between the blue and red lobes, is that the transition in geometry results from a projection effect in a gas moving with constant speed along the walls of a conical shell. In this scenario, it is the difference in the radial component of the velocity vector at different positions of the shell which produces the apparent change in geometry as a function of velocity: the low-velocity maps show the gas from the shell that is moving near the plane of the sky and that will be distributed with a V shape, while the high-velocity maps show the gas in the back side of the shell (where the radial velocity component is higher) and the emission will appear concentrated along the axis. In § 4.2.2 we will further elaborate on this interpretation and we will present a simple geometrical model to support it.

Not all the gas distribution in the maps is explained with a simple conical shell model, and at large distances from the IR cluster a systematic deviation from the shell geometry occurs. Near $\Delta\delta \approx -100''$ there is a weak extension of the ^{13}CO emission to the east in the $14 < V < 16$ and

$16 < V < 18$ maps, and the outflow gas seems to change direction, first moving northeast and later southeast. These oscillations in the outflow direction have been previously noticed by Bally et al. (1987), who mapped the ^{12}CO emission and described them as similar to the "meandering" of a river. As these authors suggests, the oscillations probably originate from the outflow encountering dense gas along its path once the flow is outside the core.

3.2. *Results from* ^{12}CO *Observations*

In order to study the fastest outflow gas, we present in Figure 4 a series of velocity maps of the more abundant ^{12}CO isotope. Because of the high optical depth of ^{12}CO in the Mon R2 outflow and the presence of strong self absorption at ambient velocities (see, e.g., Loren 1977), only the very high-velocity regime can be studied with this molecule. Still, a comparison between the ^{12}CO maps and the ^{13}CO maps of the previous section shows that the two emissions are in very good agreement and that the main features seen in ^{13}CO are also recognizable in ^{12}CO.

The only feature that appears in ^{12}CO but not in ^{13}CO is a compact, extremely blue component at $(-100'', -40'')$. This component dominates the emission from about -10 to 0 km s^{-1} and is the only feature in the first two panels of Figure 4 (note that for space reasons the figure starts at -6 km s^{-1}). This blue peak differs from the clumps of the ^{13}CO maps in its large velocity extent and position outside the shells, and reminds more of the northern red gas, that was identified with an independent bipolar outflow. It is therefore likely that there is an additional outflow around $(-100'', -40'')$, although no clear candidate for an exciting source appears in the near infrared images of Hodapp (1994) and Aspin & Walther (1990b). The position however, coincides with an enhancement of the CS emission (see § 3.3.2), suggesting that a deeply embedded object may be present. Further observations are needed to confirm the outflow nature of this blue feature.

At less extreme blue velocities ($V > 2$ km s^{-1}), the ^{12}CO emission agrees well with the ^{13}CO emission of Figure 3 and the same clumps that we found in the rare isotope

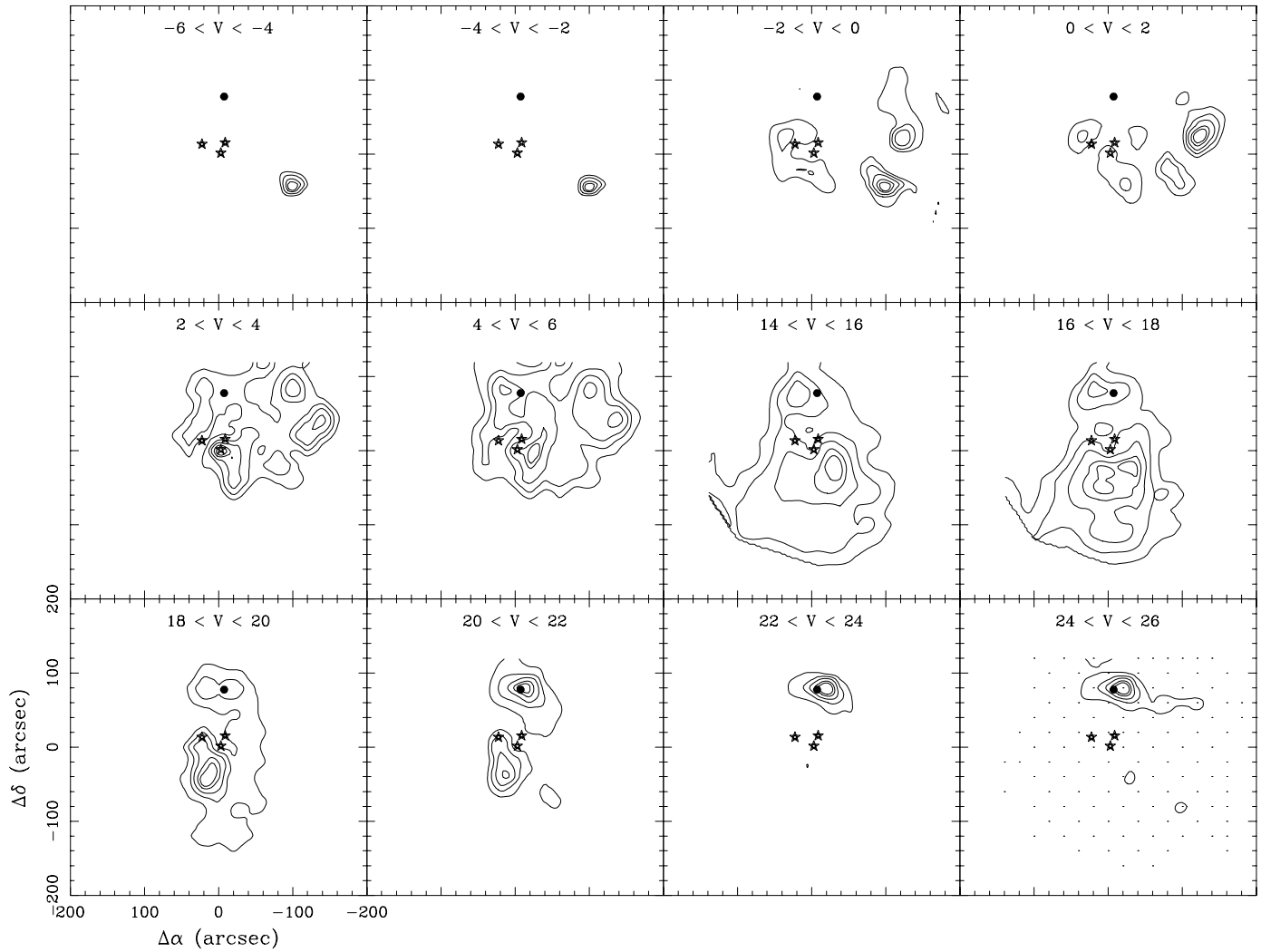


FIG. 4.—Maps of ^{12}CO(2–1) main beam brightness temperature integrated every 2 km s^{-1}. The contours of each panel are at 20%, 40%, 60%, 80%, and 90% of the map maximum, except for the first two, where the 20% contour was excluded. (Map maxima, for increasing velocity intervals, are: 4.4, 5.0, 4.6, 9.3, 20.1, 47.7, 80.5, 54.6, 48.0, 28.7, 18.0, and 9.1 K km s^{-1}.) Note that the velocity range from 6 to 14 km s^{-1} has been excluded because of its high optical depth and contamination with emission from the off position. Map centers and stars as in Fig. 1. The filled circle at $(-7''.5, 77''.5)$ indicates the position of Cohen & Frogel's (1977) Object 1.

appear in the main species at the same velocities and positions. Because of the higher intensity of ^{12}CO(2–1), the extended emission is more prominent, but the overall impression is still that of ^{13}CO: the blue lobe forms a clumpy shell of gas.

The ^{12}CO emission at ambient velocities is very optically thick and the spectra have a deep self-absorption at about 11.4 km s^{-1} (Loren 1977). For this reason, the velocity range between 6 and 14 km s^{-1} is not presented in the figure, and the following maps present the red regime.

The slow red ^{12}CO emission also resembles the slow red ^{13}CO, although the higher optical depth and the coarser sampling makes the ^{12}CO features less distinct. The distribution of red ^{12}CO is extended at low velocities with a somewhat triangular shape, and it evolves into an elongated feature as the velocity increases, in the same way the ^{13}CO emission did. As it was discussed in § 3.1.3, this change in the geometry probably results from the red outflow gas moving along the walls of a conical cavity. At the highest velocities ($V > 20$ km s^{-1}), the Mon R2-N outflow emission (see § 3.1.3) dominates and is the only feature in the last two maps.

In summary, our maps show that the ^{12}CO and ^{13}CO emissions agree well in their distribution and that all differences between them are attributable to the much larger optical depth of the main isotope. The ^{12}CO emission, in fact, is so thick that the rarer isotope is a more clear tracer of the outflow gas than ^{12}CO.

3.3. *Results from CS Observations*

As we did with the ^{13}CO emission, we study the CS kinematics in three stages of increasing velocity resolution. We first discuss the integrated maps, then the broadband maps, and finally the narrow-velocity maps.

3.3.1. *Integrated Maps: the Hourglass-shaped Cavity*

Figure 5 shows the maps of integrated intensity for CS(2–1), (3–2), and (5–4), which were observed simultaneously with the IRAM 30 m telescope. The maps in the two lowest CS transitions have the same sampling, while the CS(5–4) map has a coarser grid because the transition was substituted by ^{12}CO(2–1) in the middle of the observation.

The three CS transitions show similar brightness distributions: the two condensations east and west of IRS 1-2 and the emission valley in between. This distribution is very similar to the CS distributions found by other authors with lower resolution (see Heyer et al. 1986; Xie 1992) and to the distribution of ^{13}CO presented in § 3.1.1. Compared with the integrated ^{13}CO map (Fig. 1), the CS images show more contrast and a better definition of the condensations and the valley, that result from the lower optical depth of CS and its higher selectivity to dense gas.

In § 4.1.1 we will solve the radiative transfer of the CS lines and determine the gas density and CS column density as a function of position. However, it is not necessary to solve numerically any equation to understand qualitatively the physical difference between the condensations and the valley, and this can be done from a simple inspection of the CS maps. As these maps show, the brightness contrast between the valley and the condensations is approximately the same in all CS transitions (about a factor of 2), and because of this, the ratio between any two CS transitions is almost the same both in the valley and in the condensations. The CS emission is optically thin (§ 4.1.1), so this similar intensity ratio in the condensations and the valley implies that the excitation temperature of the CS levels is approximately the same in both regions. This means that the weaker emission along the valley has to arise from a lower CS optical depth there, that is, from a lower CS column density (about a factor of 2). It is unlikely that the lower CS column density results from an anomalous CS abundance along the valley because the valley is seen not only in CS but in many other dense gas tracers, like NH_3 (Montalbán et al. 1990), HCO^+, and HCN (Richardson et al. 1988). It is more likely that it represents a real decrease in the amount of high-density gas.

The deficit of dense gas along the valley could result from having two independent cores (the condensations) close to each other, so the valley would represent a gap between two unrelated cores. This interpretation, however, seems rather

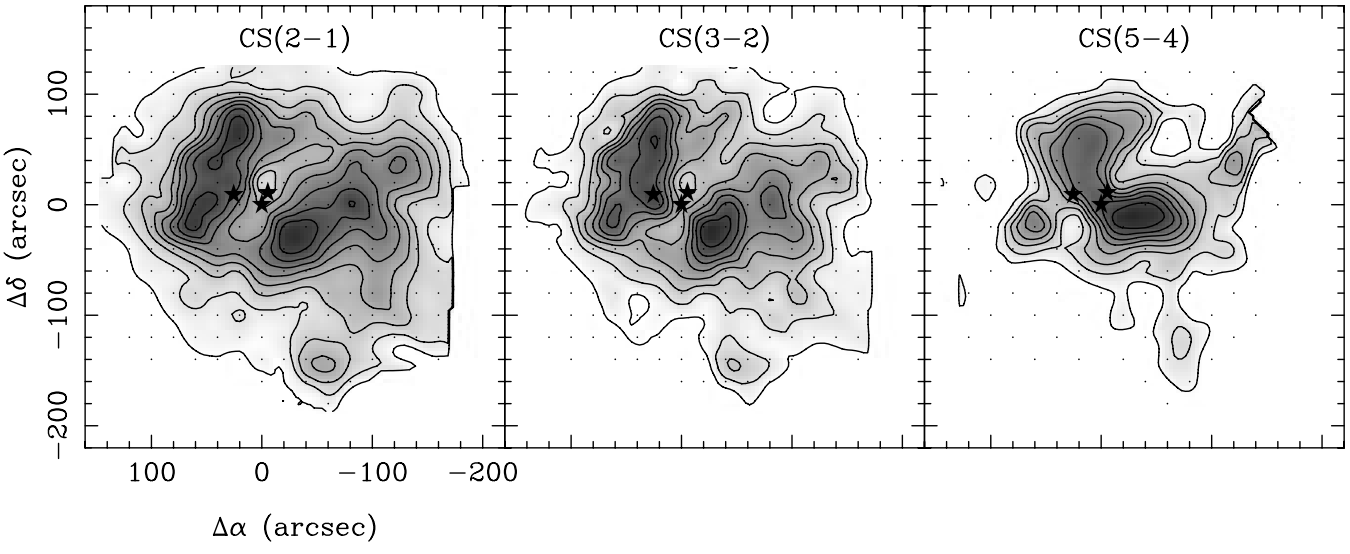


FIG. 5.—Integrated main beam brightness temperature maps (0 to 18 km s^{-1}) of CS(2–1), CS(3–2), and CS(5–4). The contours are at 20%, 30%, ..., 80%, and 90% of map maximum, and the map maxima are 25.6, 35.6, and 19.7 K km s^{-1}, for CS(2–1), (3–2), and (5–4), respectively. Map centers and stars as in Fig. 1.

unlikely because of the similar velocity of the condensations and the high symmetry of the valley, which in the integrated maps (especially the CS(3–2) one, with the highest signal-to-noise ratio) is narrower toward IRS 1-2 and broadens away from the stars with an almost constant opening angle of about 15° (with respect to the axis). This gas distribution with a high degree of bilateral symmetry, both with respect to the southeast-northwest axis and to an axis perpendicular to it, suggests that the valley is really a cavity that crosses the core from side to side and has an hourglass shape with the waist toward IRS 1-2. The axis of this cavity approximately coincides with the axis of the CO outflow, and this already suggests that outflow and cavity are related. To further investigate this connection, we need to study the velocity structure of the dense gas.

3.3.2. *Broadband Kinematics: the Shells and the Cavity*

Figure 6 presents the maps of CS(3–2) integrated intensity for the blue, ambient, and red regimes. Equivalent maps for CS(2–1) and CS(5–4) have similar features and are not presented here. The velocity ranges in the figure are similar to those used in the ^{13}CO analysis, but the ambient panel now covers only 1 km s^{-1} at each side of the central velocity, instead of the 2 km s^{-1} used for ^{13}CO, because the higher selectivity of CS to dense gas and its lower optical depth avoid confusion with the extended ambient cloud and isolate better the core emission. This ambient panel shows that the stationary dense gas lies in the condensations east and west of IRS 1-2, so the map resembles the integrated map of Figure 5.

The blue and red maps, on the other hand, show that the accelerated dense gas follows a bipolar pattern very similar to that seen in the ^{12}CO and ^{13}CO images, indicating that the CS emission also traces gas accelerated by the outflow. The blue CS map (*left panel*) is in remarkably good agreement with the blue ^{13}CO map of Figure 2 and shows the same arc-shaped distribution with even the same string of clumps. This good agreement between the ^{13}CO and CS emissions reinforces the idea that the blue outflow lobe forms a limb-brightened shell and also indicates that the outflowing material is rather dense ($n_{H_2} \geq 10^5$ cm^{-3}), as it is able to excite the CS(3–2) line. The red CS map (*right panel*) also shows a shell that is in good agreement with the ^{13}CO shell seen in the red narrow maps of Figure 3, confirming our earlier interpretation that the red lobe forms a shell. In addition, the red CS map shows an extension to the west with a well defined secondary peak at around (−100″, −20″). The position of this peak coincides with the position of the extremely blue feature of the ^{12}CO maps, which was suggested may represent an additional outflow in the field. The presence of this condensation suggests that there may be a young embedded object, even if it is too obscured to have an NIR counterpart.

It is interesting to note that the outflow shells coincide in position and orientation with the walls of the hourglass-shaped cavity that appears in the integrated CS maps. This positional coincidence suggests that the molecular outflow moves along the cavity walls, a result that agrees with the analysis of Meyers-Rice & Lada (1991), who need to assume that the gas moves along shells in order to reproduce their lower resolution ^{12}CO position-velocity diagrams. Our CS images, in fact, suggest that the outflow shells *are* the walls of the cavity, and that the cavity itself results from the evacuation of dense gas along the path of the outflow. These ideas will be further elaborated in § 4.3.3, after we have estimated the density and energetics of the outflow and the core.

3.3.3. *Detailed Kinematics: the Clumps Revisited*

In § 3.1.3 we studied the velocity maps of ^{13}CO and found that the northern shell was composed of distinct gas clumps moving at different velocities. Now, using the higher selectivity of CS to dense gas, we find that clumps are also present in the southern shell and are, in fact, a common feature of all the accelerated dense gas. The physical properties of these clumps were studied with a multitransitional CS analysis in Tafalla et al. (1994), where densities and masses for almost a dozen of them were estimated. Here, we concentrate our attention on the clump kinematics and on the distribution of clumps along the outflow shells.

Figure 7 presents a series of maps of CS(3–2) intensity integrated every 1.5 km s^{-1} covering the range with detected CS emission. The selection of the velocity intervals in Figure 7 was made to show as much detail as possible and differs slightly from that of the ^{13}CO(2–1) maps, although common features in the maps of the two molecules can be easily identified. Overall, the CS distribution appears very clumpy at the outflow velocities (both red and blue) and more extended near the ambient regime.

The two bluest maps (velocities less than 6 km s^{-1}) are dominated by a clump located near (−140″, 40″) which corresponds to clump B in the nomenclature of Tafalla et al.

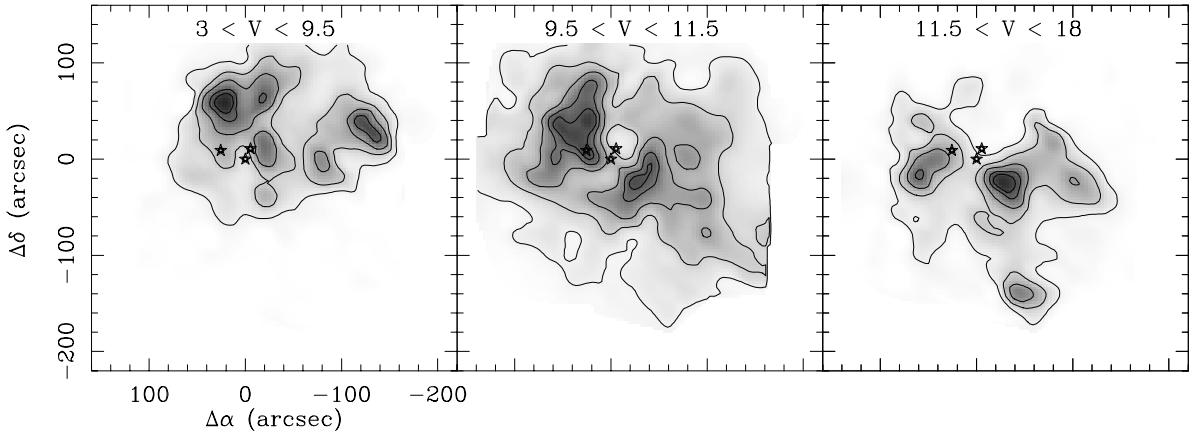


FIG. 6.—Broadband CS(3–2) velocity maps of Mon R2. The velocity range of each map is indicated in the top of the panel, and the contours are at 20%, 40%, 60%, 80%, and 90% of the map maximum (map maxima are 12.7, 19.4, and 12.4 K km s^{-1}). Map centers and stars as in Fig. 1.

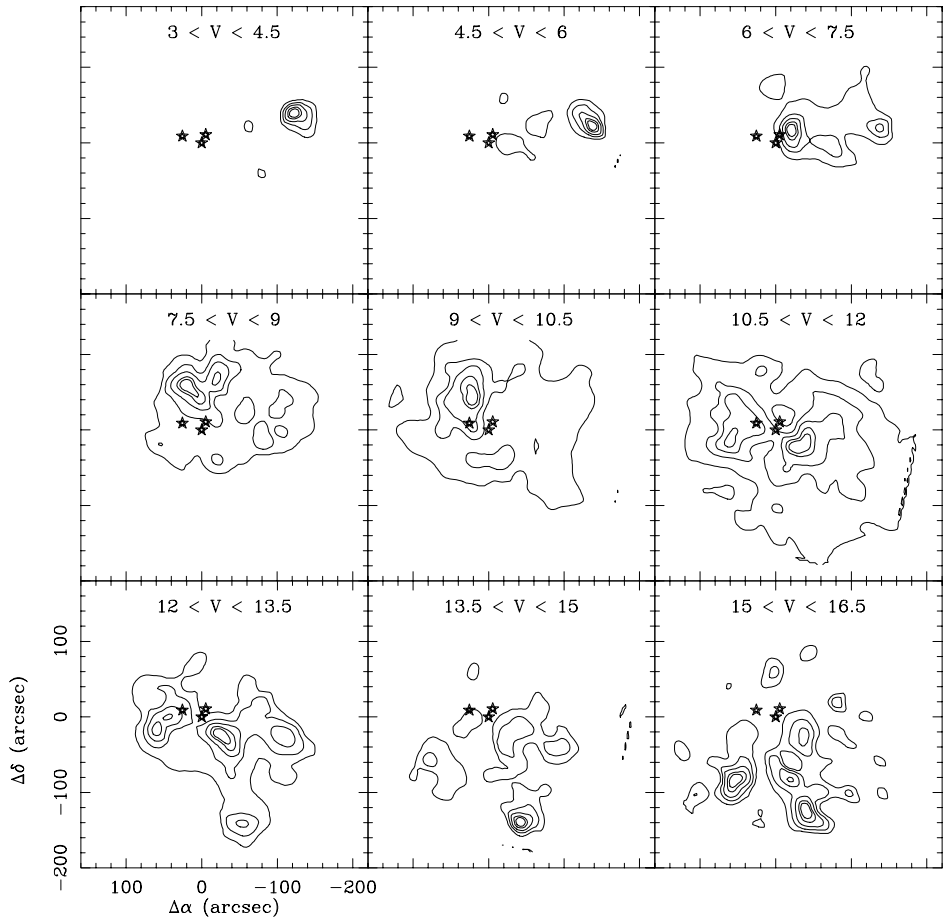


FIG. 7.—Maps of CS(3–2) intensity integrated every 1.5 km s^{-1}. The contours in each panel are at 20%, 40%, 60%, 80%, and 90% of the map maximum. (Maxima are 2.8, 3.5, 4.7, 6.9, 19.6, 16.4, 5.3, 2.5, and 1.4 K km s^{-1}.) Map center and stars as in Fig. 1.

(1994). This clump seems to move slightly between the two maps, probably because of the superposition of two different clumps with somewhat different velocities, as indicated by the presence of two distinct secondary components in the spectra (see Fig. 2 in Tafalla et al. 1994). Between 6 and 7.5 km s^{-1}, the emission from clump B weakens substantially, and a new clump appears at (−20″, 20″). This clump (C) is one of the brightest and coincides with a local minimum in the ambient line emission, as if, at this position, an appreciable fraction of the dense gas (about half) had been transferred from the ambient to the outflow regime.

At velocities closer to the ambient value ($7.5 < V < 9$ map), new clumps appear along the eastern side of the shell, showing the same trend we found in ^{13}CO that faster clumps lie in the western side of the shell while the slower clumps appear toward the east. Although this gradient could suggest rotation, it does not have a counterpart in the south, and most likely originates from a slowing down of the gas toward the east because of the presence of more dense gas in that direction as seen in the integrated maps.

The maps for $9 < V < 10.5$ and $10.5 < V < 12$ km s^{-1} present the distribution of the ambient gas (the core systemic velocity is ≈ 10.5 km s^{-1}). These two maps show that the condensation east of the IR cluster has a velocity gradient along the outflow direction, with blueshifted gas to the north and redshifted gas to south (a result previously found by Heyer et al. 1986). The western condensation, on the other hand, only appears in the second map, and seems to be slightly redshifted with respect to the systemic velocity. Overall, the extended emission changes from north to south as the velocity changes from blue to red, reflecting that the outflow velocity field is present in the dense gas even at the lowest velocities.

The red maps ($V > 12$ km s^{-1}) show that the southern shell is also made up of clumps. In the first red map ($12 < V < 13.5$), the main two peaks coincide with the southern tips of the condensations seen at ambient velocities, illustrating the continuity between the ambient and outflow regimes. Also, the secondary peak that coincides with the extremely blue ^{12}CO emission is clearly prominent to the west. At redder velocities, the emission appears more concentrated, and individual clumps along the southern shell dominate the maps. As in ^{13}CO, there is a trend for the walls of the southern shell to approach each other with increasing velocity, but unfortunately the CS emission disappears before reaching the velocities at which ^{13}CO forms a single feature at the center. The transition from shell to centrally concentrated geometry, therefore, seems present in the CS data, but its detection is incomplete because of the weakness of the emission.

In summary, the narrowband velocity maps show that bipolar outflow motions dominate the kinematics of the dense gas in Mon R2. Even at ambient velocities the dense gas continues the pattern of the outflow, so it seems that a previous interpretation of Mon R2 as a rotating toroid (Torrelles et al. 1983; Richardson et al. 1988; Wolf et al.

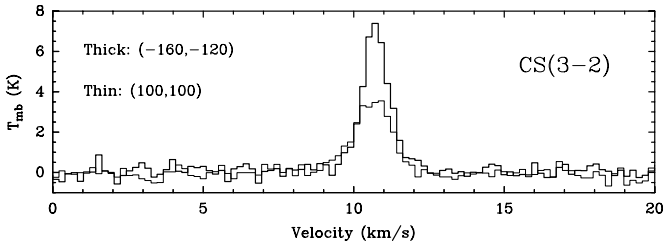


FIG. 8.—CS(3–2) spectra for two extreme positions along the putative Mon R2 rotating toroid. Note the good agreement between the line velocities that indicates the lack of any significant large-scale rotational component in the velocity field of the dense gas.

1990, but see Torrelles et al. 1990 for an interpretation in terms of outflow acceleration) results from a confusion of this outflow motion with a rotation pattern when the core is observed at low angular resolution. To further illustrate how little importance, if any, solid-body rotation has on Mon R2, we present in Figure 8 the spectra from two positions located far enough from the cluster so that the outflow effect is negligible. The positions lie at the two extremes of the putative rotating toroid, but the two lines coincide in velocity to better than a channel. Our observations, therefore, show that the Mon R2 core is expanding with the bipolar outflow, and not rotating around it.

4. DISCUSSION

4.1. *Physical Parameters of the Molecular Gas*

4.1.1. *Volume and CS Column Density of the Ambient Gas*

In order to separate the ambient and outflow contributions in the CS spectra and estimate independently the physical properties of the two regimes, we fit a Gaussian to the line at each position masking the high-velocity channels. We consider the fit results to represent the ambient emission, while the high-velocity residual represents our best guess for the outflow emission. The ambient component is usually well defined and can be separated from the outflow, but at some positions the spectrum consists of a broad Gaussian that could result from either slow outflow or random turbulence in the ambient cloud. In these cases, we have fitted a single component to the spectrum and associated all the emission to the ambient cloud, so our analysis will tend to underestimate the amount of outflow gas.

The intensities from the CS(2–1) and CS(3–2) fits at each point (the CS(5–4) data were not used because of their coarser coverage and lower signal-to-noise ratio) were compared with the intensities from a grid of 2,000 isothermal, homogeneous cloud models, the radiative transport of which was solved using the LVG approximation (see Castor 1970; Goldreich & Kwan 1974). The cloud was assumed isothermal with a temperature of 40 K as suggested by the ammonia analysis of Montalbán et al. (1990), and the CS collisional coefficients were kindly provided by S. Green (see Turner et al. 1992 for more details). The best model fit for each intensity pair was found by searching among the models in a grid of density and CS column density until finding the one that was in closest agreement with the observations. A further interpolation between models was carried out to improve the accuracy.

The results from inverting the intensities of each cloud position are presented graphically in Figures 9 and 10. Figure 9 shows the spatial distribution of CS column density as a function of right ascension and declination.

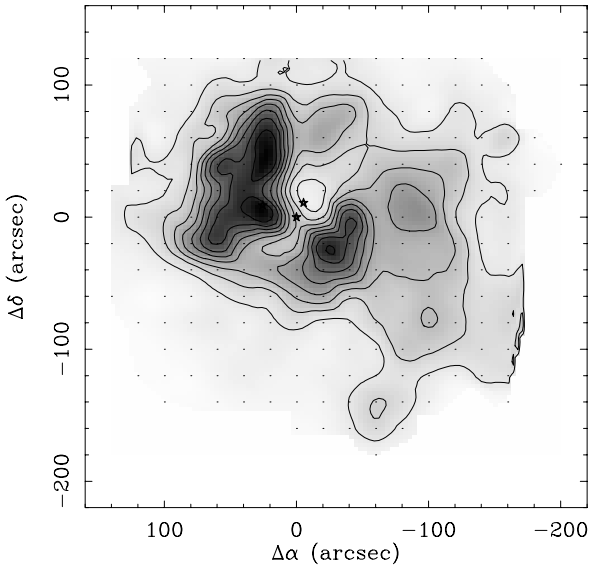


FIG. 9.—Map of CS column density derived from an LVG analysis of the CS(2–1) and CS(3–2) ambient lines. Contours are at 20%, 30%, ..., 90% of map maximum (1.4×10^{14} cm^{-2}). Compare to the integrated intensity maps of Fig. 5.

This distribution is almost indistinguishable from that of the CS integrated intensity presented in Figure 5, as it shows the condensations at each side of the IR sources and the valley between them. Even the widening of the valley with increasing distance to the cluster and the condensation to the southwest are present in the map of column density as they were in the maps of integrated intensity. The more accurate LVG analysis, therefore, validates our qualitative conclusions in § 3.3.1: the two condensations at each side of the IR cluster represent maxima in the CS column density, while the emission valley is a region with deficit of dense gas.

The volume density, on the other hand, does not present such a systematic distribution, and a map of this quantity

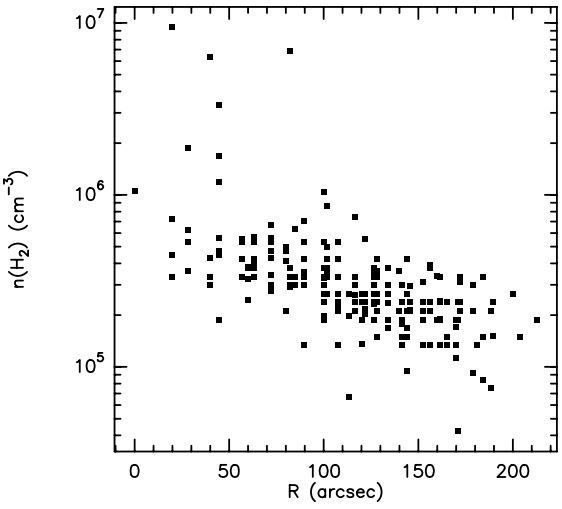


FIG. 10.—Distribution of the gas volume density as a function of distance to the Mon R2 center as derived from an LVG analysis of the CS(2–1) and CS(3–2) lines. Except for a few outlier points with $n > 10^6$ cm^{-3} (for which the 2–1/3–2 ratio is not very sensitive and uncertainties in n are very large), the volume density remains approximately constant in the inner 100″, and then decreases almost linearly with distance to the core center.

lacks of any recognizable feature like the valley or the condensations. Figure 10 presents the volume density as a function of distance to the center of Mon R2, defined as the map center of the previous figure. Discarding the points where the density is much larger than 10^6 cm^{-3} (for which the 2–1/3–2 ratio is not very sensitive and uncertainties are large), the density appears almost constant inside the central 100 arcseconds, with a typical value of 4×10^5 cm^{-3}. This is also in good agreement with our qualitative analysis of § 3.3.1, where we found that the excitation temperature (and therefore density) remains almost constant over the core. Only at large distances from the cluster, the density seems to drop slowly, decreasing almost linearly by about a factor of 2 between 100 and 200 arcseconds. It is important to note, however, that the value of the density in the inner part of the core is very close to the critical density of the CS lines, and this suggests that the constant value may arise from a thermalization of the CS lines and not from a real lack of density gradient in the inner part. A more detailed multitransitional analysis of the CS emission, using higher excitation lines, will be presented in Choi et al. (1997).

4.1.2. *Density of the Accelerated Gas*

In Tafalla et al. (1994) we fitted Gaussians to the secondary components at selected clump positions and we analyzed the emission with the LVG approximation just as we have done for the ambient gas. In this way, we determined volume densities for the accelerated clumps between 2×10^5 and 7×10^5 cm^{-3}. These clump densities are very close to the densities we have now derived for the ambient cloud, and the agreement supports the conclusion of Tafalla et al. (1994) that the accelerated clumps have densities similar to that of the surrounding core. The study of Tafalla et al. (1994), however, could only be carried out for those selected positions where the spectrum shows a well defined secondary component (clump) that allows a Gaussian fit. Unfortunately, in most places the outflow contribution appears as a wing to the ambient line, and it is not possible to derive the emission parameters from Gaussian fits. An alternative approach is therefore needed, and in this section we average the CS spectra over large regions of the core and estimate the mean density of the accelerated gas as a whole.

Even in the brightest clumps, the accelerated CS emission is optically thin (see Table 1 of Tafalla et al. 1994), so we can safely assume that the accelerated gas is optically thin in CS everywhere. This allows us to estimate the gas volume density directly from the ratio of two CS lines, assuming the kinetic temperature is known. By taking line ratios, in addition, we can study the volume density as a function of velocity, with the advantage that relative variations of the ratio across the spectrum are free from calibration errors.

In order to increase the signal to noise of the intensity ratio, we separate the study of the blue and red wings, and we calculate the ratios using only spectra with strong outflow emission. For the blue outflow, we select the 34 positions with strongest blue emission (integrated CS(3–2) intensity between 6 and 9 km s^{-1} larger than 3 K km s^{-1}), produce the average CS(2–1) and CS(3–2) spectra, and then take their ratio. The result is illustrated in the top panel of Figure 11 ("BLUE" label), where both the combined CS(2–1) spectrum (thin line) and the CS(2–1)/CS(3–2) ratio (thick line) are presented. The intensity ratio is almost constant from about 5.5 to 8 km s^{-1}, and only deviates by about 20% from the ambient value of ≈ 0.8, while the CS(2–1) intensity decreases by a factor of 5. Unless a gradient of temperature with velocity exactly cancels the effect of a density gradient, the "BLUE" panel indicates the blue-shifted gas does not change significantly its density with velocity (at least for $V_{LSR} \geq 5$ km s^{-1}) and retains its ambient core value.

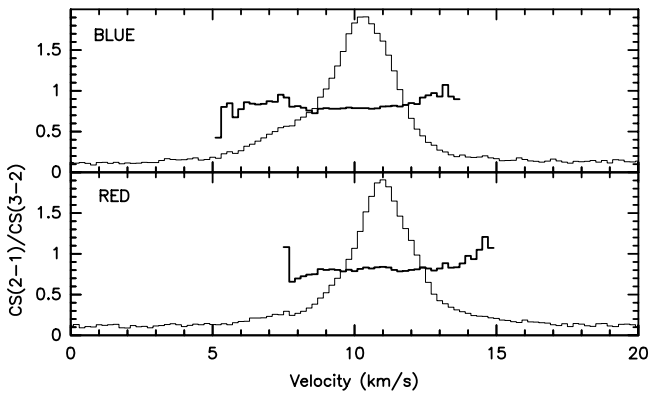


FIG. 11.—*Solid line*: CS(2–1)/CS(3–2) ratio of average spectra as a function of velocity. *Thin line*: average CS(2–1) spectrum (intensity scale not plotted). For the "BLUE" panel, only positions with integrated CS(3–2) blue intensity (from $V_{LSR} = 6$–9 km s^{-1}) larger than 3 K km s^{-1} were used. For the "RED" panel, only positions with integrated CS(3–2) red intensity (12–15 km s^{-1}) larger than 3 K km s^{-1} were used.

The ratio for the red wing presents a similar behavior. The bottom panel of Figure 11 ("RED" label) shows the ratio between the average of the 18 spectra with strongest red emission (integrated CS(3–2) intensity between 12 and 15 km s^{-1} larger than 3 K km s^{-1}). Again, the 2–1/3–2 ratio remains almost constant, while the CS(2–1) intensity (thin line) decreases rapidly. Between 12 and 14 km s^{-1}, the CS(2–1) emission decreases by more than a factor of 5, while the 2–1/3–2 ratio increases by 20% at most. If this change were due to a density variation, the density in the redshifted gas would only need to decrease by less than 40% from its value at ambient velocities.

If both the red and blue (2–1)/(3–2) line ratios do not vary across the spectrum, it seems safe to conclude that the gas excitation does not depend on velocity, at least in the first few km s^{-1} of the outflow regime traced in CS. This is most simply understood if both the temperature and density do not change and retain their ambient values. If we assume that the gas kinetic temperature is 40 K (Montalbán et al. 1990) and that the outflow gas is optically thin, the 2–1/3–2 intensity ratio found in the lower two panels of Figure 11 (≈ 0.8) implies a gas density of about 3.5×10^5cm^{-3}. This density is in good agreement with the densities estimated for the outflow clumps (Tafalla et al. 1994), suggesting that the clumps are representative portions of outflow gas and not density enhancements in a lower density outflow. It is also in good agreement with the density of the ambient core we have derived in the previous section, suggesting that the high-velocity CS emission arises from core gas that has been set into motion by the outflow.

4.1.3. *CS Abundance in the Accelerated Gas*

Although carried out with different telescopes, the ^{13}CO and CS observations were done using the same map center and grid spacing, so we have a large number of Mon R2 positions with spectra from both molecules. The angular resolution for these spectra are rather similar (24″ for CS(2–

1), 16″ for CS(3–2), and 22″ for ^{13}CO(2–1)), so it is possible to compare the emission from the two molecules at common positions, and use the fact that the emission is optically thin at outflow velocities to derive the ^{13}CO/CS relative abundance in the accelerated gas.

Again, in order to enhance the signal-to-noise ratio of the data, we separate the study of the blue and red gas, and average the spectra from different positions following the same method we used in the density analysis. Figure 12 shows the CS(3–2) spectrum (thin line) and the ^{13}CO(2–1)/CS(3–2) ratio as a function of velocity (thick line) for the same two averages that we used in Figure 11. In both panels, the ^{13}CO(2–1)/CS(3–2) ratio presents a minimum at the ambient velocity ($V_{\rm LSR} \approx 10.5$ km s^{-1}) and increases toward the outflow regime where it remains almost constant. The contrast between the ratio at ambient velocities and at the ^{13}CO(2–1) half maximum is less than 0.5, and it most likely results from the finite optical depth of ^{13}CO(2–1) at the line center rather than from an abundance gradient in the outflow. For example, if the optical depth of ^{13}CO(2–1) at the line center is 1, the intensity there will be reduced from its optically thin value by $(1 - e^{-\tau})/\tau = 0.63$, so the ratio between ^{13}CO(2–1) and any optically thin line would be reduced by the same amount. (If $\tau = 2$, the above factor is 0.43.) A moderate optical depth at the line center, in fact, was already suggested when studying the distribution of ^{13}CO(2–1) at ambient velocities (§ 3.1.2).

In the blue wing (top panel), between $V_{\rm LSR} = 8$ and 6 km s^{-1}, the ^{13}CO/CS ratio remains approximately constant with a value of ≈ 6 until it is affected by a low-level ripple in the ^{13}CO(2–1) spectrum that contaminates the data and limits the velocity range we can study. In the red wing (bottom panel), the ratio also remains at a level of about 6, in good agreement with the blue wing.

To estimate the ^{13}CO/CS abundance ratio from the intensity ratio, we assume the two emissions at outflow velocities are optically thin and arise from gas of density 3.5×10^5 cm^{-3} (see § 4.1.2) and kinetic temperature 40 K. In the optically thin regime, the emitted CS intensity will be proportional to the CS column density, but because of the high-dipole moment of CS, there is no guarantee that LTE conditions will hold, so the proportionality factor between integrated intensity and column density has to be calculated explicitly. To do so, we solve the statistical equilibrium equations in the optically thin limit, determine the excitation temperatures of all levels, and from them, derive the partition function. As a result,

$$N(\mathrm{CS}) = 3.1 \times 10^{12} \int T_B^{\mathrm{CS}(3-2)}\, dV \ \mathrm{cm}^{-2} .$$

In a similar way for ^{13}CO (where LTE holds), we derive

$$N(^{13}\mathrm{CO}) = 6.8 \times 10^{14} \int T_B^{^{13}\mathrm{CO}(2-1)}\, dV \ \mathrm{cm}^{-2} ,$$

with T_B in Kelvin and V in km s^{-1}. The intensity ratio between ^{13}CO(2–1) and CS(3–2) is independent of velocity, so the ratio of the integrated intensities is equal to the ratio of peak intensities, that we assume to be 6. In this way, we obtain $N(^{13}\mathrm{CO})/N(\mathrm{CS}) = 1.3 \times 10^3$. From this ratio, and using a ^{13}CO abundance of 2×10^{-6} (Dickman 1976), we estimate a CS abundance of 1.5×10^{-9}. This value is in good agreement with other CS abundance determinations for high-mass star-forming regions, like that of Zhou et al. (1991) for the NGC 2071 core (2×10^{-9}), and although it differs from what Blake et al. (1987) estimate for the Orion outflow (2.2×10^{-8}), it is rather similar to their estimate for the ridge (2.5×10^{-9}). The CS abundance in Mon R2, therefore, seems not to be appreciably enhanced in the outflow gas.

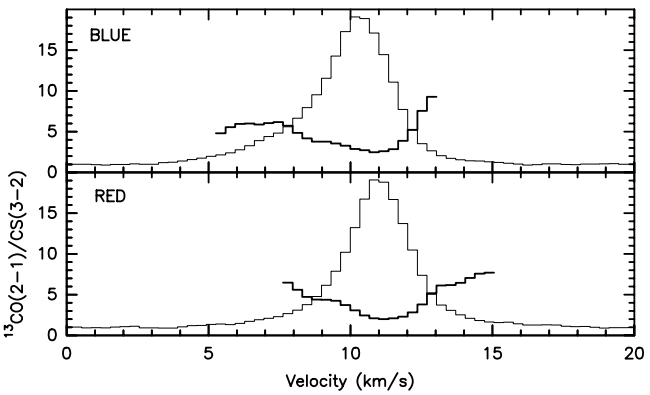


FIG. 12.—*Solid line*: ^{13}CO(2–1)/CS(3–2) ratio of average spectra as a function of velocity. *Thin line*: average CS(3–2) spectrum (intensity scale not plotted). "BLUE" and "RED" averages as in Fig. 11.

4.1.4. *Mass Estimate of the Core: Ambient and Accelerated Components*

After estimating CS column densities for the ambient cloud at each point in our maps (§ 4.1.1) and deriving an average CS abundance for all velocities (§ 4.1.3), we can now estimate the mass of the ambient component in the dense core over the area we have mapped (see Fig. 5). For each observed position, we convert the CS column density into an H_2 column density and then we add the contribution of all core positions. In this way, we estimate the mass of the stationary gas in the dense gas to be 850 $M_\odot$.

To estimate the mass of the accelerated component, we integrate the residuals of the spectra after subtracting the Gaussian fits used to determine the ambient emission. As the accelerated CS is optically thin, we convert the integrated CS intensities into CS column densities for each position by using the relation we derived in the previous section. Assuming again a CS abundance of 1.5×10^{-9}, we estimate the mass of the accelerated dense gas to be ≈ 170 $M_\odot$. This amount of accelerated dense gas is (coincidentally) the same than what Russell et al. (1992) derive for the DR 21 outflow, showing that although extreme, Mon R2 is not an isolated case but a typical representative of the outflows from high-mass stars.

The above mass estimates for the ambient and accelerated components of the dense gas indicate that in the Mon R2 core, from a total of ≈ 1000 $M_\odot$ of dense gas, more than 15% has already been set in motion by the outflow. This is in fact an underestimate of the outflow effect on the core, as our method of separating the ambient and outflow components by fitting gaussians to the spectra tends to treat part of the low-velocity outflow as turbulent stationary ambient gas (see § 4.1.1).

4.2. *Outflow Kinematics*

4.2.1. *Energy and Momentum in the Outflow Gas*

Determining the energy parameters of an outflow involves large uncertainties because of the difficulty in converting the observed radial velocities into their real three-

dimensional values (see, e.g., Cabrit & Bertout 1990). Following Margulis & Lada (1985), we estimate the outflow energetics using two extreme angle corrections that bracket the real outflow parameters. The first correction supposes that all the outflow gas moves at the maximum observed velocity, and assumes that all intermediate velocities in the spectra arise from the projection of this maximum velocity onto the line of sight; in this way an upper limit to the outflow energetics is derived. From the ^{12}CO velocity maps (§ 3.2), we estimate that the maximum outflow speed is 10 km s^{-1}, and using the mass estimate of the outflow gas derived from the ^{13}CO data (275 $M_\odot$, see below), we derive a total momentum and energy of $P = 2,750 M_\odot$ km s^{-1}, and $E = 2.7 \times 10^{47}$ erg. These values are in good agreement with those of Wolf et al. (1990) who, using the same method, estimated the momentum and energy of the outflow as 2,400 $M_\odot$ km s^{-1} and 2.9×10^{47} erg. The agreement, in fact, is better than it should be, as Wolf et al.'s estimate applies to the whole Mon R2 outflow, while ours considers only its central part. It probably results from a compensation of our smaller region with the fact that our ^{13}CO observations allow us to probe velocities lower than those studied by Wolf et al. in ^{12}CO.

The second method of estimating the outflow energetics applies no angle correction to the velocity, and assumes that the observed radial component is the real, three-dimensional value; in this way, the outflow parameters are underestimated. To apply this method, we first convert the ^{13}CO(2–1) intensity at each position into a mass column density, assuming that the outflow emission is optically thin, the ^{13}CO abundance is 2×10^{-6} (Dickman 1976), and the excitation temperature is 40 K (Montalbán et al. 1990). We then add the contributions from all positions, each multiplied by the surface area covered by the beam; the result gives the distribution of molecular mass as a function of velocity. To subtract the ambient cloud contribution, we fit a Gaussian to the central 3 km s^{-1} of the distribution, and take the excess emission over this Gaussian as representing the accelerated outflow gas. The results of this estimate are presented in Table 1, which shows a total momentum in the outflow of 1.1×10^3 $M_\odot$ km s^{-1} and a total energy of 5.2×10^{46} erg. It should be noticed that the outflow mass estimate in the table is larger than the mass estimate of the accelerated dense gas we derived from the CS data (§ 4.1.4) because of the larger spatial coverage of the ^{13}CO observations. Given our incomplete mapping of the outflow, even this ^{13}CO mass estimate is still a lower limit.

Comparing the two methods of deriving the outflow energetics, we conclude that the Mon R2 outflow carries a momentum of 1.1–2.7×10^3 $M_\odot$ km s^{-1}, and has a kinetic energy of 0.5–2.7×10^{47} erg. In addition, our estimates suggest that the red lobe contains 2 times more mass than the blue lobe, 3 times more momentum, and 4 times more energy. This does not necessarily mean, however, that the total Mon R2 outflow is asymmetric, as our energy estimate only applies to the central part. Wolf et al. (1990) have shown that the outflow extends over a larger area than that we have mapped, and that it contains a separate blue component northwest of the IR cluster that lies outside our maps. It is possible that this component contains enough energy and momentum to compensate for the asymmetry observed in the central region.

TABLE 1

OUTFLOW ENERGETICS (NO CORRECTION FOR PROJECTION EFFECTS)

Parameter	Blue	Red	Total
Mass ($M_\odot$).....	80	195	275
P ($M_\odot$ km s^{-1}).....	279	809	1088
E (ergs).....	1.1×10^{46}	4.1×10^{46}	5.2×10^{46}

4.2.2. *A Geometrical Model for the Outflow*

In § 3.1.3 we interpreted the transition in geometry from shell to centrally concentrated that so systematically appears in the ^{13}CO(2–1) velocity maps as resulting from a projection effect. We argued that if the outflow gas moves along a conical shell, the emission at low velocities will come from the intersection of the shell with the plane of the sky, and its distribution will look like an inverted "V". At high velocities, on the other hand, the emission will come from the back of the shell, where the radial component is largest, and the emission will appear concentrated along the outflow axis. Here, with the help of a simple geometrical model, we prove that this is the case.

Our model is similar to that described by Meyers-Rice & Lada (1991) and used by these authors to analyze position-velocity diagrams in the Mon R2 outflow. It assumes that the outflow gas moves along two opposed parabolic shells that emerge from the exciting star. The gas travels with constant density and constant excitation. LTE conditions are assumed, given the low-dipole moment of ^{13}CO, and the emergent intensity is calculated by computing the column density of gas at different velocity intervals. The gas column densities are converted into optical depths by multiplying by the opacity at a fiducial line of sight, that is left as a free parameter. A more detailed description of the model is given in Tafalla (1993).

As an example of the type of results the model produces, we present in Figure 13 a comparison between one model calculation and the observed ^{13}CO(2–1) emission. The bottom panels represent the three velocity intervals in which the red outflow changes from shell to centrally concentrated geometry (see also Fig. 3), and the top panels represent the model results for the same three velocity intervals. For this particular model, we assume that the outflow velocity is 10 km s^{-1} and the outflow axis is inclined 30 degrees from the plane of the sky (following Meyers-Rice & Lada 1991). As the figure shows, the geometrical model reproduces reasonably well the observed change in geometry without the need for an acceleration or a change in the velocity field. The variations in the geometry arise naturally from projection effects.

If our model is correct, we should expect to see the front side of the shell at low velocities. Unfortunately, the velocity range at which this should occur coincides with the range at which the much brighter ambient emission dominates the maps, so if present, the front side contribution would be lost in the much brighter ambient background.

4.3. *Outflow-Core Interaction*

4.3.1. *Comparison of Outflow Kinetic Energy and Core Gravitational Energy*

In § 3.3.2 we argued that the Mon R2 outflow has evacuated the cavity that crosses the dense core. In order to do that, the outflow must be energetic enough to overcome part of the core binding energy, and in this section, we compare the outflow kinetic energy with the core gravita-

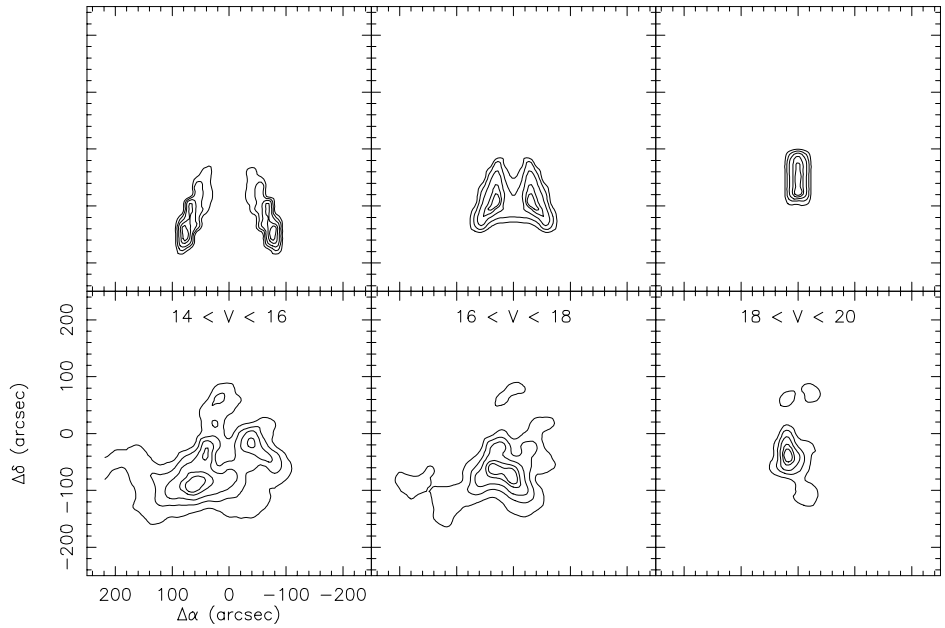


FIG. 13.—Comparison between the velocity maps predicted by a geometrical model (*top*) and the observed ^{13}CO(2–1) emission at the same velocities (*bottom*). Note the transition between a shell-like geometry at low velocities, to a centrally concentrated geometry at high velocities. Contours are at 20%, 40%, ..., 80%, 90% of the map maximum for each panel.

tional energy to test our interpretation. Because of the large uncertainties in the outflow energetics, core mass, etc., the comparison between the two quantities is necessarily approximate. In particular, we ignore the possible binding effect of the embedded stellar cluster and that of any atomic gas that may be present.

We estimate the core binding energy by assuming that the dense gas is distributed spherically. The gravitational energy of a sphere of radius R and mass M is $\alpha GM^2/R$, where α is of order unity ($\frac{3}{5}$ for an homogeneous sphere and 1 for a r^{-2} density profile; see, e.g., MacLaren, Richardson, & Wolfendale 1988). From the CS maps (see Fig. 5), we estimate the core radius is 0.35 pc (75″ at 950 pc), and use the core mass value derived in § 4.1.4 ($\approx 10^3\ M_\odot$). With these parameters, the core binding energy ranges between 2.4×10^{47} and 1.4×10^{47} erg (for $\alpha = 1$ and 3/5, respectively).

The estimate of the outflow kinetic energy is subject to a large uncertainty, and in § 4.2.1 we calculated two extreme values that probably bracket the real kinetic content of the flow (at least in its inner part). These values (0.5×10^{47} and 2.7×10^{47} erg) are very close to the core binding energy estimated below, showing that in principle, the bipolar outflow has enough kinetic energy to affect the core. In fact, the outflow kinetic energy we have measured represents energy that has *already* been deposited onto the ambient cloud, because the molecular outflow consists of ambient gas that has been swept up. This means that the outflow has deposited on its surroundings an amount of energy comparable to the binding energy of the whole core. It is very likely, therefore, that it has affected the core structure by opening the hourglass cavity seen in the CS maps.

4.3.2. *Line Width Enhancement of the Ambient Gas*

In § 4.1.1 we fitted Gaussians to the central velocity range of the CS spectra and used the intensities from the fits to derive properties of the ambient gas. In this section we use the same fits to study the changes in the ambient gas velocity dispersion by analyzing the dependence of the fitted line width with position. Figure 14 presents the CS line width at each point in our maps as a function of distance to the infrared cluster. The line widths in the figure are geometrical means of the full widths at half maximum derived from Gaussian fits to the CS(2–1) and CS(3–2) spectra after the outflow velocities were masked out (the line widths of the two transitions agree better than 15% rms). They represent our best estimate of the ambient gas line width, although some bipolar outflow component is still present (see below).

The figure shows a clear trend of increasing CS line width toward the cluster. At about 200″ from the IR stars, line widths are close to 1 km s^{-1}, while in the cluster vicinity, line widths range from 2.5 to 3 km s^{-1}. Between these two extremes, the change is almost linear with distance and follows a relation of the form $\Delta V(\mathrm{km\ s^{-1}}) = 2.6 - 0.0072R(arcsec)$ (derived from a least squares fit).

Not all the line width enhancement results from an increase in the gas turbulent motions. At some positions, especially toward the eastern blue shell, the increase in line

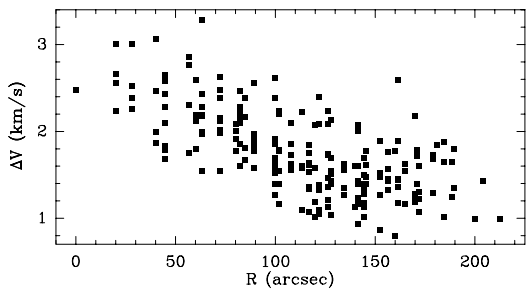


FIG. 14.—CS line width as a function of distance to the Mon R2 center. Each point represents the average of the full widths at half maximum of the CS(2–1) and CS(3–2) spectra for each position (derived from a Gaussian fit). The width increases linearly with decreasing distance to the core center, suggesting the outflow has increased the turbulence of the ambient gas in its vicinity

width does not occur symmetrically with respect to the ambient velocity, but is more pronounced in the outflow direction. The CS lines at those positions still look approximately Gaussian, but because of the additional emission at outflow velocities, the velocity centroid shifts and the line width increases. The line width enhancement toward the cluster, therefore, results from a combination of an increase of turbulent motions and low-velocity outflow.

Line width enhancement associated with bipolar outflow activity is not unique to Mon R2. Myers et al. (1988), from a survey of low-mass star-forming cores, found that cores with CO outflow have NH_3 line widths significantly larger than cores without outflows. Our Mon R2 observations prove that a similar situation holds for a high-mass star-forming region, and in addition, our high angular resolution allows us to resolve the spatial distribution of the line broadening. To test the outflow origin of this broadening, we estimate the amount of energy required to broaden the CS lines by assuming that the original line width was 1 km s^{-1} everywhere in the core (this is the line width at large distances from the cluster). At each point, we convert the ambient CS column density (derived from the LVG analysis of § 4.1.1) into a total gas mass and, multiplying by the amount of energy per unit mass needed to increase the one-dimensional velocity dispersion from 1 km s^{-1} to the observed value, we derive a total energy of 2×10^{46} erg. This energy is clearly lower than the outflow kinetic energy (§ 4.2.1), so the outflow has enough energy to produce the observed line broadening.

4.3.3. *A Unified Picture of the Mon R2 Outflow-Core System*

In the previous sections we have studied the accelerated CS emission and determined the properties of the gas that gives rise to it. We have estimated that this gas is as dense as the rest of the core and that it moves along the walls of the hourglass-shaped cavity following the pattern of the bipolar outflow. For these reasons we have sometimes referred to it as "dense outflow" and other times as "accelerated core," depending on whether we stressed its kinematics or its physical properties. In fact, there is no contradiction in using the two terms, because the CS emission arises from gas that is at the same time both core and outflow. This is better understood remembering that molecular outflows are made up of swept up ambient gas (see, e.g., Snell 1987) and that in the central part of the Mon R2 outflow (the region we have studied) the ambient gas is dense core material. It is important to stress that the "CO outflow" is not what accelerates the "CS outflow," but both the CO and CS emissions arise from the same outflow material. What accelerates the molecular material in Mon R2 is as mysterious as it is for any other bipolar outflow, and although there have been claims of detection of this agent in some objects (with H I, for example, see. Lizano et al. 1988), the nature of driving winds in outflows is still far from settled

Our interpretation of the accelerated CS emission as core gas set into motion by the outflow also helps explain the presence of the hourglass cavity and the shell distribution of the moving molecular gas. As we have seen before in § 4.3.1, the outflow has already deposited on the ambient gas an amount of energy comparable to the binding energy of the core, so it is energetically possible for the outflow to have evacuated a channel along its path, and this channel will correspond to the cavity. The outflow shells, on the other hand, naturally result from the fact that once the cavity has been evacuated, the interaction between the outflow and the core can only occur along the cavity walls, that are the interface between the two media. It is there where the core gas is now accelerated, a process that at the same time that feeds the outflow with molecular material, opens the cavity even more. The acceleration, in addition, is accompanied of fragmentation (probably via the Kelvin-Helmholtz instability), and this gives rise to the clumps that dominate the ^{13}CO and CS velocity maps. A schematic of this interpretation is presented in Figure 15.

4.3.4. *Outflows, Cavities, and the Long-Term Evolution of Dense Cores*

The case of Mon R2 illustrates the association of evacuated cavities and bipolar outflows. This is a well known property of low-luminosity systems that have been studied with more detail because of their proximity. L1551, for example, presents well-defined outflow shells in CO (Moriarty-Schieven et al. 1987; Uchida et al. 1987), and the blue shell (the one approaching us) coincides with the edge of a cavity revealed by the presence of scattered light (Moriarty-Schieven et al. 1987). A similar case is that of L43, where Mathieu et al. (1988) found that the blue outflow lobe coincides with a stellar reflection nebula and a cavity seen in the NH_3 maps. The association of outflows with cavities, however, is not limited to low-luminosity systems, and other high-luminosity sources in addition to Mon R2 also illustrate this effect. Campbell, Persson, & McGregor (1986), for example, found that the blue lobe of GL 490 coincides with a conical nebula of scattered light, suggesting that the outflow moves along an evacuated channel. A case even more similar to Mon R2 is that of NGC 2071, where

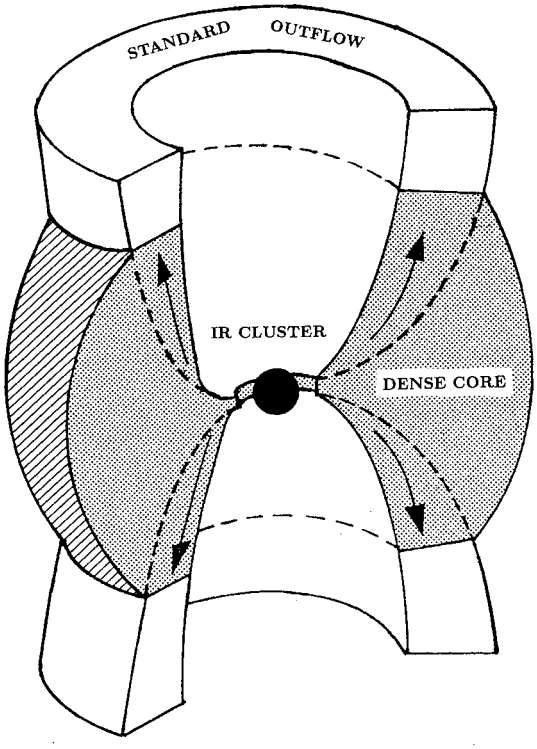


FIG. 15.—Schematic diagram for the Mon R2 core-outflow system (adapted from Fukui 1989). The bipolar outflow driven by the IR cluster has excavated a cavity in the dense core and the accelerated molecular gas moves along the cavity walls giving rise to a shell. In its inner part, the molecular outflow consists of dense gas from the core that has been set into motion.

Moriarty-Schieven et al. (1989) found well-defined outflow shells in CO, and Kitamura et al. (1990) not only traced these shells in CS, but found they contain well-defined clumps that appear as secondary components in the spectra, just like the clumps in Mon R2 appear in our data (see Tafalla et al. 1994).

This general similarity between the morphology of high- and low-luminosity outflows argues that all outflows share a common origin and follow a similar evolution, an idea that was suggested by Lada (1985) based on the relation between outflow and central source parameters, which connects in a continuous manner the outflows from low-luminosity sources with those of very luminous stars. The common association of cavities and outflows, in addition, suggests that the presence of a bipolar outflow represents a major perturbation of the stellar environment, both in the case of high- and low-luminosity systems. It may be still too soon to decide whether bipolar outflows are powerful enough to produce the full disruption of star-forming cores, but observations like those of Mon R2 already show that outflows can disperse a significant fraction of the dense gas around newly formed stars, and that their effect cannot be ignored when studying the kinematics of this gas and the long term evolution of star-forming cores.

5. SUMMARY

We have presented ^{13}CO, ^{12}CO, and CS observations of the central part of Mon R2 and studied the dense core, the outflow, and their mutual interaction. The main results of our study are the following:

1. The ^{13}CO data show that the outflow gas is distributed in two opposed limb-brightened shells that have the IR cluster near the apex and open approximately toward the north and south. When looked with sufficient velocity resolution, these shells break up into small clumps that follow the outflow pattern but move with slightly different velocities.

2. The high-velocity maps of ^{12}CO and ^{13}CO show that there is a second outflow in the Mon R2 system, about 75″ north of the main cluster. This new outflow (denoted Mon R2-N) seems associated with a bright source which appears surrounded by nebulosity in NIR images.

3. The CS data show that part of the dense molecular gas in the Mon R2 core has been set into motion. This accelerated dense gas has the same distribution as accelerated ^{12}CO and ^{13}CO. It lies along two opposed limb-brightened shells, so it consists of core gas that has been incorporated into the outflow regime. The Mon R2 outflow, therefore, is fairly dense, at least in its innermost part.

4. The limb-brightened outflow shells coincide in position and orientation with the inner walls of a cavity that crosses the dense core from side to side and has the IR cluster near its center. We interpret the cavity as the result of the evacuation of a channel through the core by a bipolar stellar wind that originates from the IR cluster. The outflow shells (the proper *molecular* outflow) result from the acceleration of ambient gas by this wind, and our observations show that this process occurs along the walls of the evacuated cavity. The outflow has probably evacuated the cavity by peeling layer after layer of gas along the cavity walls.

5. From a radiative transfer analysis of the CS emission, we estimate that the Mon R2 core contains about $10^3\ M_\odot$ of dense gas, of which at least $170\ M_\odot$ have already been set into motion by the outflow. The density of this accelerated gas is very similar to the density of the more quiescent component ($\approx 4 \times 10^5$ cm^{-3}), and the ^{13}CO/CS abundance ratio is also approximately the same in the ambient and accelerated regimes ($\approx 1.3 \times 10^3$).

6. Comparing the kinetic energy of the outflow and the binding energy of the dense core, we find that they are close enough to explain the evacuation of the cavity by the bipolar outflow. In addition, the outflow is energetic enough to produce a systematic increase of the CS line width toward the outflow center. The action of the outflow, therefore, dominates the kinematics of the dense gas in Mon R2, and other velocity patterns (like rotation), if present, are of a much smaller importance.

7. The enormous effect of the outflow on the Mon R2 indicated by the evacuation of the cavity most likely results from its accumulated action over a long period of time (Mon R2 is probably one of the oldest outflows known). Our study shows that by the end of the outflow phase, a dense core can be deeply perturbed by the action of the flow. Thus, the acceleration of the dense gas by an outflow appears as a major element in the evolution of a core after star formation has taken place.

We thank the staffs of the IRAM 30 m and the JCMT for their help during the observations. M. T. acknowledges partial support from a MEC/Fulbright fellowship. M. T. and R. B. acknowledge partial support from the Spanish DGICYT grant PB93-48. Support for this work in Berkeley is from NSF grant NSF-FD93-20238.

REFERENCES

Aspin, C., & Walther, D. M. 1990a, A&A, 235, 387
———. 1990b, in Astrophysics with Infrared Arrays, ed. R. Elston (San Francisco: ASP), 288
Bachiller, R. 1996, ARA&A, 34, 111
Bally, J., Hayashi, M., Hayashi, T., Takano, T., & Tanaka, M. 1987, in Interstellar Matter, ed. J. M. Moran and P. T. P. Ho (New York: Gordon and Breach), 201
Beckwith, S., Evans, II, N. J., Becklin, E. E., & Neugebauer, G. 1976, ApJ, 208, 390
Blake, G. A., Sutton, E. C., Masson, C. R., & Phillips, T. G. 1987, ApJ, 315, 621
Cabrit, S., & Bertout, C. 1990, ApJ, 348, 530
Campbell, B., Persson, S. E., & McGregor, P. J. 1986, ApJ, 305, 336
Castor, J. I. 1970, MNRAS, 149, 111
Choi, M., Evans, II, N. J., Tafalla, M., & Bachiller, R. 1997, in preparation
Cohen, J. G., & Frogel, J. A. 1977, ApJ, 211, 178
Davies, S. R. 1992, JCMT Tech. Rep. (Astronomer's Reference Manual)
Dickman, R. L. 1976, ApJS, 37, 407
Downes, D., Winnberg, A., Goss, W. M., & Johansson, L. E. B. 1975, A&A, 44, 243
Fukui, Y. 1989, in Low Mass Star Formation and Pre–Main Sequence Objects, ed. B. Reipurth (Garching: ESO), 95
Fukui, Y., Iwata, T., Mizuno, A., Bally, J., & Lane, A. 1993, in Protostars and Planets Vol. 3, ed. E. H. Levy & J. I. Lunine (Tucson: Univ. of Arizona Press), 603
Gilmore, W. 1980, AJ, 85, 912
Goldreich, P., & Kwan, J. 1974, ApJ, 189, 441
Gonatas, C., Palmer, P., & Novak, G. 1992, ApJ, 398, 118
Hackwell, J. A., Grasdalen, G. L., & Gehrz, R. D. 1982, ApJ, 252, 250
Heyer, M. H., Snell, R. L., Goldsmith, P. F., Strom, S. E., & Strom, K. M. 1986, ApJ, 308, 134
Hodapp, K. W. 1987, A&A, 172, 304
———. 1994, ApJS, 94, 615
Kitamura, Y,. Kawabe, R., Yamashita, T., & Hayashi, M. 1990, ApJ, 363, 180
Kutner, M. L., & Tucker, K. D. 1974, BAAS, 6, 341
———. 1975, ApJ, 199, 79
Lada, C. J. 1985, AR&A, 23, 267
Lizano, S., Heiles, C., Rodríguez, L. F., Koo, B.-C., Shu, F. H., Hasegawa, T., Hayashi, S., & Mirabel, I. F. 1988, ApJ, 328, 763

Loren, R. B. 1977, ApJ, 215, 129
———. 1981, ApJ, 249, 550
Loren, R. B., Peters, W. L., & Vanden Bout, P. A. 1974, ApJ, 194, L103
MacLaren, I., Richardson, K. M., & Wolfendale, A. W. 1988, ApJ, 333, 821
Margulis, M., & Lada, C. J. 1985, ApJ, 299, 925
Massi, M., Felli, M., & Simon, M. 1985, A&A, 152, 387
Mathieu, R. D., Benson, P. J., Fuller, G. A., Myers, P. C., & Schild, R. H. 1988, ApJ, 330, 385
Mauersberger, R., Guélin, M., Martín-Pintado, J., Thum, C., Cernicharo, J., Hein, H., & Navarro, S. 1989, A&AS, 79, 217
Meyers-Rice, B., & Lada, C. J. 1991, ApJ, 368, 445
Montalbán, J., Bachiller, R., Martín-Pintado, J., Tafalla, M., & Gómez-González, J. 1990, A&A, 233, 527
Moriarty-Schieven, G. H, Snell, R. L., & Hughes, V. A. 1989, ApJ, 347, 358
Moriarty-Schieven, G. H., Snell, R. L., Strom, S. E., Schloerb, F. P., Strom, K. M., & Grasdalen, G. L. 1987, ApJ, 319, 742
Myers, P.C., Heyer, M., Snell, R. L., & Goldsmith P. F. 1988, ApJ, 324, 907
Racine, R., & van den Berg, S. 1970, in IAU Symp. 38, The Spiral Structure of Our Galaxy, ed. W. Becker & G. Contopoulos (Dordrecht: Reidel), 219
Richardson, K. J., White, G. J., Monteiro, T. S., & Hayashi, S. S. 1988, A&A, 198, 237
Russell, A. P. G., Bally, J., Padman, R., & Hills, R. E. 1992, ApJ, 387, 219
Snell, R. L. 1987, in IAU Symp. 115, Star Forming Regions, ed. M. Peimbert & J. Jugaku (Dordrecht: Reidel), 213
Snell, R. L., Loren, R. B., & Plambeck, R. L. 1980, ApJ, 239, L17
Tafalla, M. 1993, Ph.D. thesis, Univ. California at Berkeley
Tafalla, M., Bachiller, R., & Wright, M. C. H. 1994, ApJ, 432, L127
Thronson, H. A., Jr., Gatley, P. M., Sellgren, K., & Werner, M. W. 1980, ApJ, 237, 66
Torrelles, J. M., Ho, P. T. P., Rodríguez, L. F., & Cantó, J. 1990, ApJ, 349, 529
Torrelles, J. M., Rodríguez, L. F., Cantó, J., Carral, P., Marcaide, J., Moran, J. M., & Ho, P. T. P. 1983, ApJ, 274, 214
Turner, B. E., Chan, K.-W., Green, S., & Lubowich, D. A. 1992, ApJ, 399, 114
Uchida, Y., Kaifu, N., Shibata, K., Hayashi, S. S., Hasegawa, T., & Hamatake, H. 1987, PASJ, 39, 907
Willson, R. F., & Folch-Pi, F. J. 1981, AJ, 86, 1084
Wolf, G. A., Lada, C. J., & Bally, J. 1990, AJ, 100, 1892
Xie, T. 1992, Ph.D. thesis, Univ. Massachusetts at Amherst
Zhou, S., Evans, II, N. J., Güsten, R., Mundy, L., & Kutner, M. L. 1991, ApJ, 372, 518